

PAPER • OPEN ACCESS

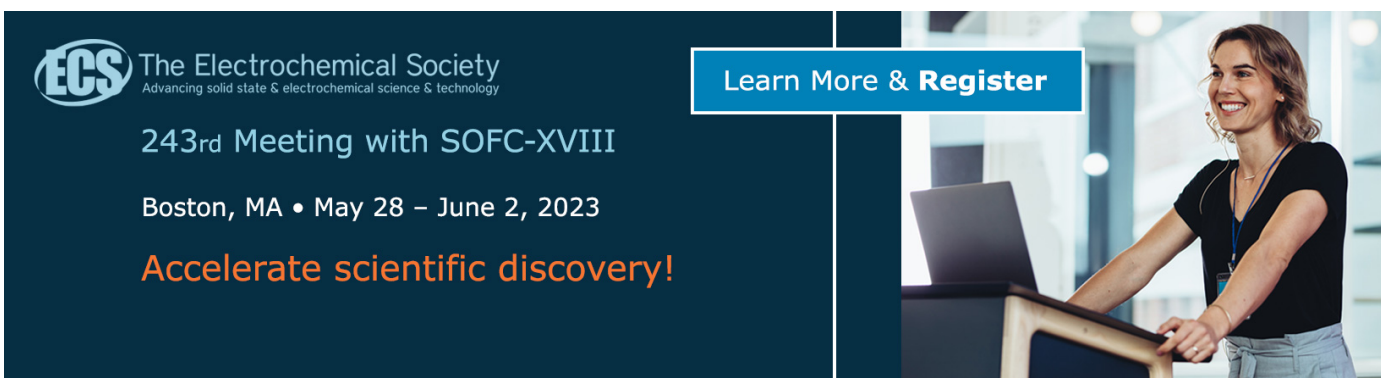
Additive manufacturing of hydroxyapatite: effect of some stereolithography parameters on the dimensional accuracy of green, debinded and sintered parts with different geometries

To cite this article: A Schrijnemakers *et al* 2023 *J. Phys.: Conf. Ser.* **2487** 012042

View the [article online](#) for updates and enhancements.

You may also like

- [The effect of debinding and sintering parameters on the mechanical and microstructural properties of Fe-2Ni metal injection molded compacts](#)
Ali Askari, Mohammad Hossein Alaei, Khanali Nekouee et al.
- [Binder removal by a two-stage debinding process for powder injection molding Fe-50Ni alloy parts](#)
Muhammad Ali, Faiz Ahmad, Puteri Sri Melor et al.
- [Widely accessible 3D printing technologies in chemistry, biochemistry and pharmaceuticals: applications, materials and prospects](#)
Evgeniy G. Gordeev and Valentine P. Ananikov




The Electrochemical Society
Advancing solid state & electrochemical science & technology

243rd Meeting with SOFC-XVIII

Boston, MA • May 28 – June 2, 2023

Accelerate scientific discovery!

Learn More & Register



Additive manufacturing of hydroxyapatite: effect of some stereolithography parameters on the dimensional accuracy of green, debinded and sintered parts with different geometries

A Schrijnemakers^{1,2}, B Vertruyen¹, D Coibion¹, R Closset¹, R Hastir¹ and F Boschini¹

¹ GREENMAT, CESAM Research Unit, Department of Chemistry, University of Liege, 4000 Liege, Belgium

² corresponding author: aschrijnemakers@uliege.be

Abstract. We report on the stereolithography printing of a hydroxyapatite powder dispersed in an acrylate-based resin with a focus on the influence of the laser power, the scanning speed and the layer thickness on the dimensional accuracy of the green, debinded and sintered parts and on the microstructural and mechanical properties of the sintered parts.

1. Introduction

“Additive manufacturing” includes a wide range of production technologies allowing the layer-by-layer construction of three-dimensional objects, starting from a digital 3D model. By comparison with subtractive machining manufacturing methods, additive manufacturing techniques bring fundamental changes to the way objects and devices are designed. They provide versatility and flexibility for the customization of high value-added products.

Beyond the initial focus on prototyping and research, the contributions of additive manufacturing in a production context are now widely recognized for (i) the diversity and complexity of shapes compared to traditional processes, (ii) the possibility of manufacturing a wide range of custom parts using a single machine, (iii) the reduction in labor costs thanks to process automation and (iv) the possibility of local production through a rapid transfer of knowledge between manufacturing sites thanks to digitalization and computer-aided design [1]. To cite a few examples, additive manufacturing techniques are already used by major car manufacturers to produce engine components, the Food and Drug Administration has approved the use of 3D printed implants and the International Space Station has a 3D printing machine to manufacture parts and components in space [2].

Most of the additive manufacturing techniques applied to ceramics rely either on a powder-bed process or on slurry/paste processes. The latter ones allow to avoid the high cost of the mold machining in classical slurry-based forming techniques and include methods such as robocasting, fused deposition of ceramics, ceramic material jetting, ceramic stereolithography (SLA) or ceramic digital light processing (DLP) [3]. Both the SLA and the more recent DLP techniques are vat photopolymerization techniques, based on the local curing of a polymeric resin containing the ceramic powder and a photo-initiator. Since the beginnings, SLA has been recognized for its high dimensional accuracy, the surface quality of the printed parts, and its ability to print very small structures [4]. SLA printers are available in bottom-up or top-down configuration, reflecting the movement of the fabrication platform. The forces acting on the part under construction are smaller in the top-down



configuration, making it possible to obtain a better level of detail, greater precision and a smooth surface state of the finished parts.

By comparison with the SLA of polymers, the SLA of ceramics [5] is a more complex process due to the influence of the ceramic powder, whose high content in the polymeric resin impacts the reactivity of the slurry to photopolymerization, the dimensional resolution of the printed part and the need for a debinding/sintering step to obtain the final part. The ability of SLA to produce high-performance ceramics with a relative density greater than 99% but also parts with custom-controlled porosity has been demonstrated, with obvious interest for example in the production of custom-made biocompatible implants for personalized medicine [6]. However, an optimization (or, at least, a fine tuning) of the experimental parameters should be performed for each new powder; such studies also allow to progressively build a better understanding of how the physicochemical characteristics of the powder impact the powder-resin interactions during the formulation of the slurry and with the laser beam during the printing process.

Here we report on the SLA of a hydroxyapatite powder dispersed in an acrylate-based resin with a focus on the influence of the laser power, the scanning speed and the layer thickness on the dimensional accuracy of the green, debinded and sintered parts and on the microstructural and mechanical properties of the sintered parts.

2. Materials and methods

2.1. Materials

The hydroxyapatite powder HA1, made up of spray-dried granules (granulometric distribution: $d_{10} = 0.9 \mu\text{m}$, $d_{50} = 2.7 \mu\text{m}$, $d_{90} = 9.7 \mu\text{m}$), was used for most of the experiments. Another powder (HA2) with a d_{50} similar to HA1 was used for some comparison tests. The resin consisted of amine-modified polyetheracrylate oligomers. The dispersant was the phosphoric ester salt of a high molecular weight copolymer with pigment-affinic groups (BYK-Chemie GmbH, Wesel, Germany). The photo-initiator was 2,2-dimethoxy-1,2-diphenylethan-1-one (Sigma Aldrich, Gillingham, UK).

2.2. Slurry preparation, SLA printing and heat treatment

The HA1 hydroxyapatite powder was mixed with the resin and the dispersant to reach a 56 vol% powder loading. The SLA printing experiments were conducted with a CERAMAKER C900 system (3DCeram Sinto, Bonnac-la-côte, France). This printer is equipped with a pulsed diode-pumped Nd:YVO₄ laser delivering a wavelength of 355 nm thanks to frequency-tripling. Samples were printed from the same batch of slurry for different laser powers (*LP*) [60-200-340 mW], scanning speeds (*SS*) [250-500-750 cm s⁻¹] and sliced layer thicknesses (*SLT*) [50-75-100 μm]. The UV laser beam scanned the surface in parallel lines (rotated by 90° for each successive layer) with a hatching distance (i.e., distance between parallel lines) of 40 μm. 12 dense squares (15x15 mm², 3 mm thick), 6 long and 6 short bars and 3 gyroid pore networks were printed for each set of experimental parameters listed in table 1. The as-printed samples (green bodies) were cleaned with solvent and compressed air to remove the remaining non-polymerized slurry.

The green bodies were debinded according to a thermal cycle optimized from the thermogravimetric curve measured on the green parts. The sintering of the parts was carried out for 2 hours at 1230°C to avoid the formation of a liquid phase and excessive growth of the hydroxyapatite grains.

Table 1. Sets of printing parameters: *LP* = laser power, *SS* = scanning speed, *SLT* = sliced layer thickness, including 3 replicates for the set of intermediate values of the printing parameters.

<i>LP</i> (mW)	60	60	60	60	200	200	200	340	340	340	340
<i>SS</i> (cm s⁻¹)	750	750	250	250	500	500	500	750	750	250	250
<i>SLT</i> (μm)	50	100	50	100	75	75	75	50	100	50	100

2.3. Characterization

The power of the laser beam was measured using a power-meter positioned at the same height as the top layer of the part being printed. The rheological behavior of the ceramic slurry was tested with a MCR 102 rheometer (Anton Paar, Austria) with a 50 mm parallel plate geometry, varying the shear rate from 0.1 to 100 s^{-1} at a constant temperature of 21.0°C. The degree of polymerization was characterized using infrared spectra collected on the unexposed slurry and on a freshly broken cross-section of the green body with a Nicolet iS5 iD7 spectrometer in attenuated total reflection configuration.

The external X , Y , Z dimensions of the dense square parts were determined with a caliper and compared to the CAD model. For each set of printing parameters, the average and the deviation on X , Y and Z were determined from measurements on 12 (green bodies and debinded parts) or 3 (sintered parts) dense square samples. The green bodies of the gyroid pore networks were examined by scanning electron microscopy (Tescan Clara SEM, wide field mode). Surface roughness (Veeco optical profilometer) and open/closed porosity (Mettler Toledo kit for Archimedeian measurement) were measured on 6 debinded parts and 3 sintered parts for each set of printing parameters. Freshly fractured cross-sections of sintered parts were observed by SEM (Tescan Clara).

Vickers hardness was measured by applying 9.81 N (1 kgf) during 15 s to create indentations whose surface-projected diagonals were measured with an optical microscope (Instron TUKON2100, Wilson-Wolpert USA). Ten acceptable indentations were made on a representative area distributed on a diagonal of dense square parts after debinding. Measurements were collected on three different parts before calculations of the average and the error as described in ASTM C1327-03. The mechanical resistance of the printed specimens was characterized using a Zwick-Roell Z050 TH all-round test bench with a crosshead speed of 1 N s^{-1} . The specimen dimensions and test conditions were defined according to ASTM C1161-13 (bending) and ISO 17162:2014 (compression) standards. Compression and bending tests were carried out on three sintered bars for each set of printing parameters.

3. Results

3.1. HA1 powder

The SEM micrograph in figure 1a shows the microstructure of the HA1 hydroxyapatite powder, consisting of spherical granules with diameters ranging from 2 to 10 μm . This powder was mixed with the acrylate-based resin to reach a powder loading of 56 vol%, which should be high enough to ensure the mechanical strength of the parts after debinding. The rheology curve in figure 1b indicates a viscosity of 90 Pa s at 100 s^{-1} (21 °C) and displays the shear-thinning behavior needed to allow for proper recoating of each irradiated layer with a fresh layer of the ceramics-resin paste.

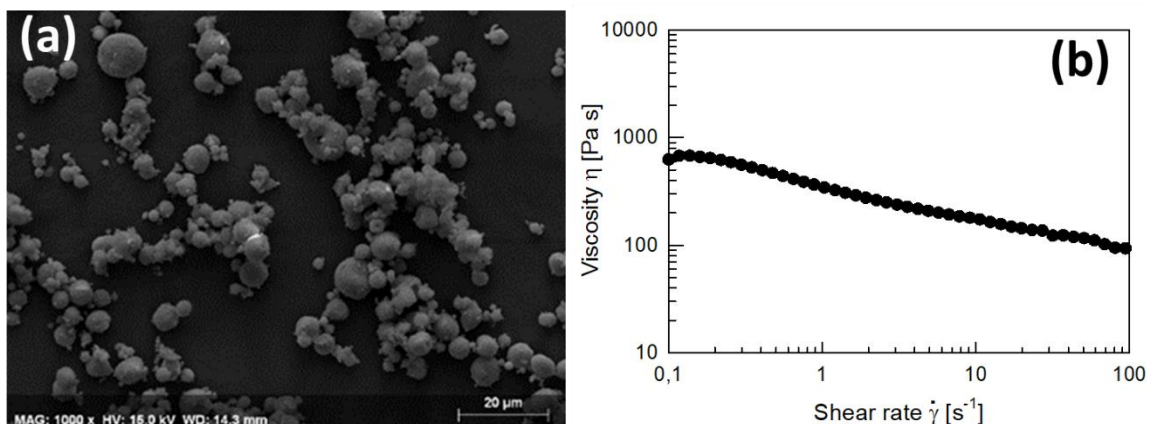


Figure 1. (a) SEM micrograph of the HA1 hydroxyapatite powder; (b) rheological curve at 21°C for the paste obtained by mixing the acrylate-based resin with 56 vol% hydroxyapatite powder.

The cure depth (CD) for each of the sets of printing parameters was evaluated by measuring the thickness of the cured layer peeled off a thick paste layer after one laser scan. These cure depth values are listed in table 2 and plotted in figure 2 as a function of the energy dose (E) calculated through the division of the laser power (LP) by the product of the scanning speed (SS) and the hatching distance (0.004 cm). With the energy dose in logarithmic scale, a linear dependence is expected according to the working curve $CD = DP \ln(E/E_c)$, where the penetration depth DP and the critical energy dose E_c are constants for the paste under investigation [5]. With a R^2 of 0.73 for the agreement between the experimental points and the linear regression, the values $DP = 120 \mu\text{m}$ and $E_c = 2.7 \text{ mJ cm}^{-2}$ should be considered as estimates.

The cure depth values are between two and twelve times larger than the smallest layer thickness; therefore, during the printing of the parts, the already scanned layers receive additional insulation. The large cure depths can be related to the high level of functionalization and amine modification of the resin, which impart it with a fast kinetics of propagation polymerization reactions.

Table 2. Printing parameters (LP = laser power, SS = scanning speed, SLT = sliced layer thickness) and the calculated or measured values of energy dose (E), cure depth (CD), degree of polymerisation (D_{polym}) and dimensions with respect to CAD model (X , Y , Z) for the green bodies of square samples.

HA1 powder								
LP (mW)	SS (cm s ⁻¹)	SLT (μm)	E (mJ cm ⁻²)	CD (μm)	D_{polym} (%)	X (%)	Y (%)	Z (%)
60	750	50	20	240	74	101.9	101.8	97.1
60	750	100	20	240	57	101.6	101.5	94.1
60	250	50	60	374	90	103	103	98.4
60	250	100	60	374	78	102.8	103.6	96.9
200	500	75	100	437	71	103.6	103.7	96.4
200	500	75	100	437	69	103.5	103.6	96.9
200	500	75	100	437	79	103.6	103.6	97.3
340	750	50	113	452	61	103.5	103.6	94.1
340	750	100	113	452	80	103.4	103.3	94.5
340	250	50	340	584	84	105.7	106.3	98.5
340	250	100	340	584	79	106.4	106.6	96.9

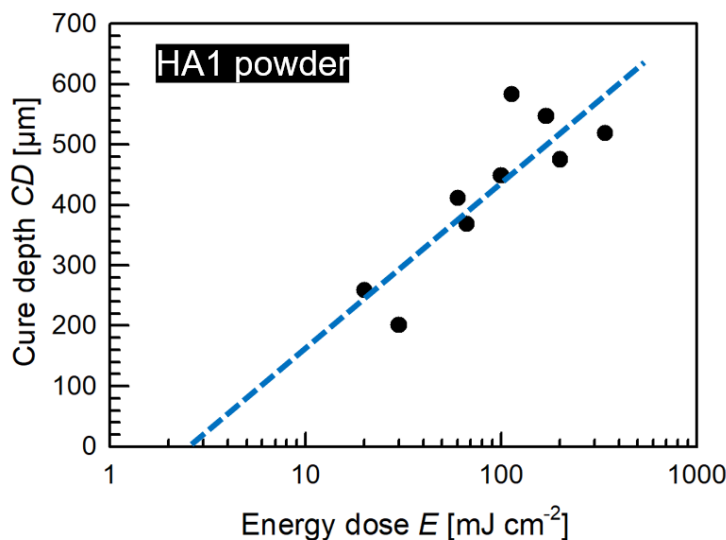


Figure 2. Cure depth CD as a function of the energy dose E for all the sets of printing parameters in table 2. The dashed blue line corresponds to the equation $CD = DP \ln(E/E_c)$ with $DP = 120 \mu\text{m}$ and $E_c = 2.7 \text{ mJ cm}^{-2}$.

Figure 3a shows the CAD models of the different geometries (square, short and long bars and gyroid porous network) printed with each set of printing parameters. For all geometries and printing conditions, green bodies with good adhesion of the layers and enough mechanical strength to withstand the cleaning of the uncured paste were successfully manufactured. Indeed, as shown in the column D_{polym} in table 2, degrees of polymerization between 61 and 90% were measured for the green bodies of the square samples.

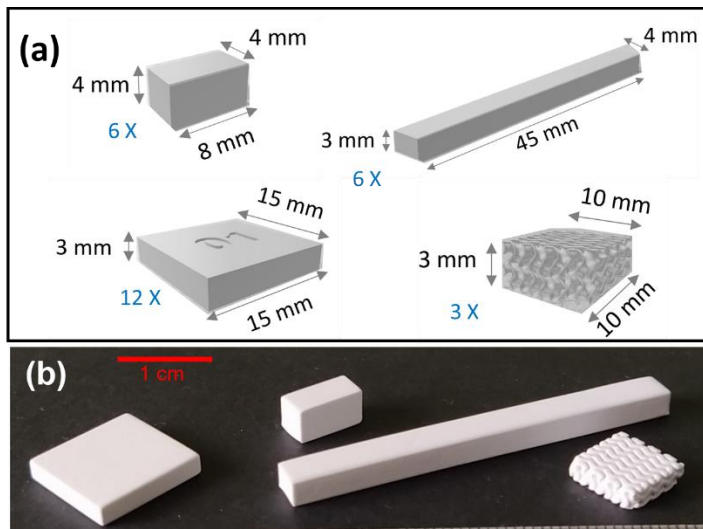
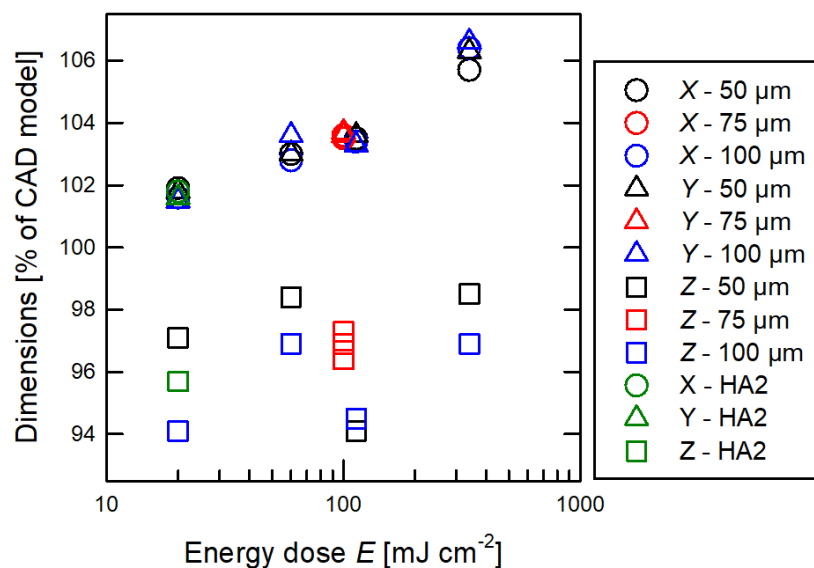


Figure 3. (a) CAD models for a square sample, short and long bars and a gyroid porous network; (b) photographs of the printed parts after debinding.

The dimensions of the green bodies of the square samples are listed in table 2 and plotted in figure 4 as percentages of the dimensions in the CAD models. The lateral dimensions (X and Y) show a positive deviation of a few percent compared to the CAD design, probably due to the lateral scattering of the laser beam by the ceramics powder; the deviation increases with the energy dose for one scan (E), while the layer thickness does not seem to affect the lateral resolution significantly. The datapoints for the test with the HA2 powder agree with the general trend. The thickness dimensions (Z) show negative deviations by 2 to 4 %; the Z datapoints in figure 4 do not reveal a clear trend, possibly due to an experimental error introduced when detaching the parts from the building platform.

Figure 4. Lateral dimensions (X , Y) and thickness (Z) of the green bodies of the square samples as a function of the energy dose for one scan (E). Black, red and blue symbols correspond to layer thicknesses (SLT) of 50, 75 and 100 μm , respectively. Green symbols correspond to results of the test with the HA2 powder and a layer thickness of 100 μm .



A more severe test of the dimensional accuracy was performed by printing gyroid porous networks. The CAD model shown in figure 3 was deliberately created with unrealistically thin walls, so that the actual samples reflect the best attainable resolution for each set of printing parameters. Figure 5 shows low-magnification SEM micrographs of the green bodies. As expected, the fine structure becomes increasingly blurred for higher energy doses per scan (from left to right in figure 5). Since the cure depth is larger than the layer thickness, a smaller layer thickness is associated to a higher cumulated energy dose and the resulting additional blurring is observed when going from 100 μm layers to 50 μm layers (from top to bottom in figure 5).

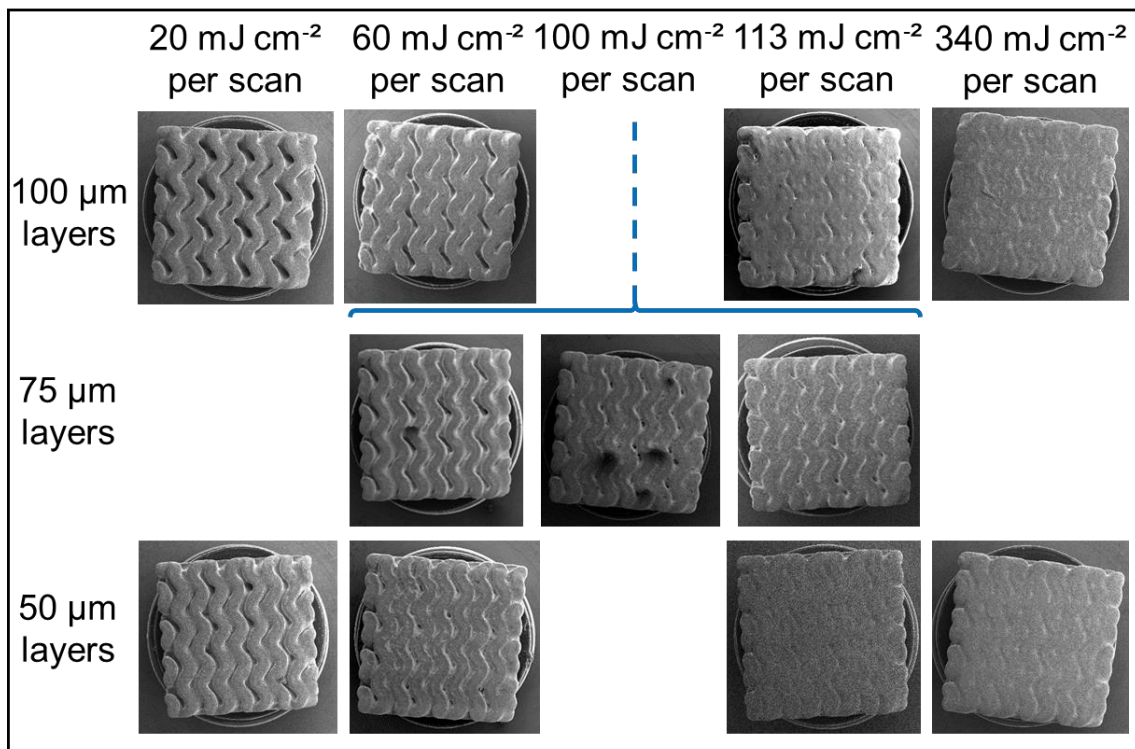


Figure 5. Low magnification SEM micrographs of the green bodies of the gyroid porous networks, organized by increasing energy dose per scan (from left to right) and decreasing layer thickness (from top to bottom). The edge of the square face of the green bodies is 1 cm long.

The dimensions of the green bodies evolved during the debinding and sintering treatments. The shrinkage measured on the square samples was similar for all sets of printing parameters: with respect to the dimensions of the green bodies, the shrinkage was about -3.5% after the debinding treatment and between -17.5 and -18% after sintering at 1230°C for 2 hours.

The porosity of the pieces reflects the densification taking place during the sintering treatment, going from open porosities between 38 and 40% for the debinded parts to residual closed porosities of about 2.5 % after sintering. Figure 6 illustrates the post-sintering microstructure with a typical micrograph of a freshly fractured cross-section. The surface rugosity of the sintered pieces was characterized by optical profilometry, with root mean square height (S_q) values of $\sim 2 \mu\text{m}$.

Finally, the debinded and sintered parts were submitted to mechanical testing. The Vickers hardness HVI of the debinded square samples ranged between 10.5 and 12.5 (± 0.5) while the compressive strength and flexural strength measured on the short and long bars, respectively, reached $158 \pm 14 \text{ MPa}$ (compressive strength) and $94 \pm 4 \text{ MPa}$ (flexural strength).

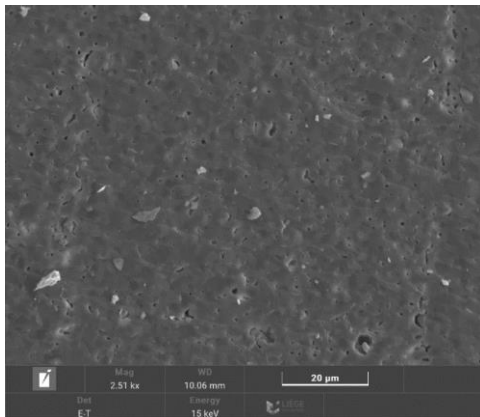


Figure 6. SEM micrograph of a typical freshly fractured cross-section through a square sample sintered at 1230°C for 2 hours.

3.2. HA2 powder

For comparison, some of the experiments were also carried out using the hydroxyapatite powder HA2, made up of platelet-like particles (Figure 7a) with a granulometric distribution: $d_{10} = 0.6 \mu\text{m}$, $d_{50} = 2.1 \mu\text{m}$, $d_{90} = 5.8 \mu\text{m}$. As for the hydroxyapatite powder HA1, the HA2 powder was mixed with the resin and the dispersant to reach a 56 vol% powder loading. The cure depth (CD) for each of the sets of printing parameters was evaluated by measuring the thickness of the cured layer peeled off a thick paste layer after one laser scan. These cure depth values are plotted in figure 7b as a function of the energy dose (E) calculated as previously described. With a R^2 of 0.87 for the agreement between the experimental points and the linear regression $CD = DP \ln(E/E_c)$, the values $DP = 106 \mu\text{m}$ and $E_c = 2.0 \text{ mJ cm}^{-2}$ are in the same range as those obtained for the slurry based on hydroxyapatite powder HA1.

Square parts were printed from the HA2 slurry with a laser power of 60 mW, a scanning speed of 750 cm s^{-1} and a sliced layer thickness of $100 \mu\text{m}$. The dimensions of the green bodies of the square samples, expressed as percentages of the dimensions in the CAD model, are plotted as the green symbols in figure 4. The lateral dimensions ($X = 101.8 \%$ and $Y = 101.6 \%$) are identical to these measured for HA1 slurry and show a positive deviation of a few percent compared to the CAD design.

The HA1 and HA2 powders have similar d_{50} but different shapes (spherical granules and irregular agglomerates, respectively). The fact that the curing behavior and lateral broadening are similar suggests that the observed results are mostly determined by the high reactivity of the resin.

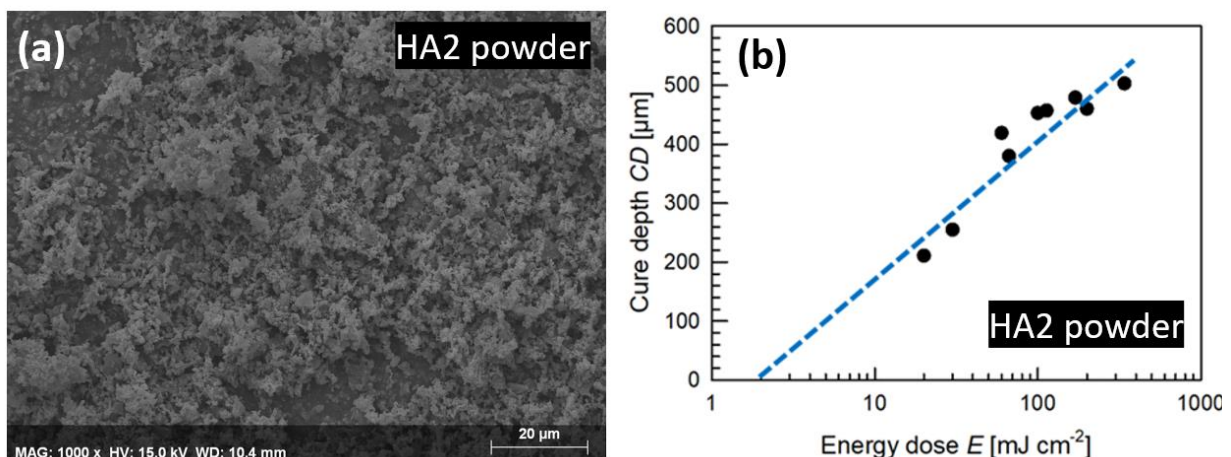


Figure 7. (a) SEM micrograph of the hydroxyapatite powder HA2; (b) Cure depth CD as a function of the energy dose E for all the sets of printing parameters in table 2. The dashed blue line corresponds to the equation $CD = DP \ln(E/E_c)$ with $DP = 106 \mu\text{m}$ and $E_c = 2.0 \text{ mJ cm}^{-2}$.

4. Concluding discussion

In the explored range of printing parameters, the cure depth after one scan and the lateral broadening of the dense square samples show a roughly linear variation with respect to the logarithm of the energy dose, in agreement with literature where the equations for the SLA of polymers are adapted to take into account the scattering by the ceramic powder grains [5].

Since the cure depth is larger than the layer thickness for all sets of printing parameters, the cumulated energy dose increases when the layer thickness decreases but we did not observe any impact of the layer thickness on the lateral accuracy of the square samples. On the contrary, the large curing depths limit the attainable spatial resolution of the gyroid networks, because most of the walls in this design are oriented obliquely to the printing direction and are broadened by both the lateral scattering and by the over-deep curing.

The large curing depths and significant lateral broadening can be related to the high reactivity of the resin. The difference in refractive index, which is known to be a factor affecting the scattering of the laser beam by the particles [5,7], is relatively small in the present case, with typical values of ~ 1.65 for hydroxyapatite [8] and ~ 1.5 for acrylate-based resins [9].

In conclusion, the lower end of the range of printing parameters explored in this work would be appropriate for the printing of dense parts or designs with relatively thick walls parallel to the printing direction. More complex geometries with smaller details require a change of resin formulation and/or a shift to lower energy doses.

Acknowledgments

This work was supported by the Walloon Region through project 1810019.

References

- [1] Garrett B 2014 *Glob. Policy* **5** 70
- [2] de Leon Al C, Chen Q, Palaganas N B, Palaganas J O, Manapat J and Advincula R C 2016 *React. Funct. Polym.* **103** 141
- [3] Peng E, Zhang D and Ding J 2018 *Adv. Mater.* **30** 1802404
- [4] Pelz J S, Ku N, Meyers M A and Vargas-Gonzalez L R 2021 *J. Mater. Res. Technol.* **15** 670
- [5] Halloran J W 2016 *Annu. Rev. Mater. Res.* **46** 19
- [6] Zocca A, Colombo P, Gomes C M and Günster J 2015 *J. Am. Ceram. Soc.* **98** 1983
- [7] Chartier T, Chaput C, Doreau F and Loiseau M 2002 *J. Mater. Sci.* **37** 3141
- [8] Holzmann D, Holzinger D, Hesser G, Schmidt T and Knör G 2009 *J. Mater. Chem.* **19** 8102
- [9] Hinczewski C, Corbel S and Chartier T 1998 *Rapid Prototyping J.* **4** 104